Demonstration of a Practical Nb_3Sn Coil for an Actively-Shielded Generator

David Loder, *Member, IEEE,* Matthew Feddersen, Reed Sanchez, Kiruba Haran, Mike Sumption, Chris Kovacs, Milan Majoros, E.W. Collings, David Doll, Xuan Peng, and Jinji Yue

***Abstract*—This paper describes a detailed design of a 6 Tesla Nb_3Sn superconducting racetrack coil designed for conduction cooling. We then describe a bench test pursued as a proof of concept for one winding of an actively-shielded, air core electric machine with superconducting field windings. Electromagnetic design selection is drawn from previous optimization work. The coil former design is then discussed. Numerical simulations of thermal and structural features are pursued to determine temperature distribution and strain within the winding. Coil instrumentation and experimental setup of a quasi-conduction cooled system is described. Finally, test results are presented; a maximum critical current of 480 A was reached at a peak temperature of 7.9 K, surpassing the operational current goal of 435 A. Future work and planned improvements to the test setup are discussed.**

***Index Terms*—AC machines, magnetic shielding, rotating machines, superconducting coils, superconducting magnets.**

I. Introduction

An actively shielded superconducting field winding topology using Nb_3Sn was proposed in [1]. Compared to conventional permanent magnets, superconducting field coils are capable of demonstrating an order of magnitude increase in energy density; previous work has indicated air-gap flux density of up to 3 T is achievable in practical designs with superconducting field windings [2]. This higher energy density coupled with the lower cost of Nb_3Sn wire can be leveraged to eliminate the heavy steel components, actively shield the external magnetic field, and achieve significant increases in magnetic loading. By employing these strategies, large increases in electric machine power density can be achieved, which is enabling for certain applications such as offshore wind and electric aircraft propulsion [3].

High-field Nb_3Sn magnets have been developed mostly within the domain of national laboratories, driven primarily by the demands of high-energy physics and nuclear fusion; fields up to 16 T have been demonstrated [4] - [6]. Recent efforts are associated with high energy physics and future upgrades to the Large-Hardron Collider (LHC); these include the MQXF quadropole coil developed by LARP, the FRECSA2 racetrack coil developed by CERN, and an 11 T dipole magnet developed by FNAL [7] - [9]. However, these coils do not face the practical challenges of more cost-sensitive large-scale applications, which must contend with the the economic realities of steeply increasing liquid helium prices [10]. In contrast, few cryogen-free coils have been demonstrated [11].

However, now the challenge lies in cooling the field windings to the required 4 to 6 K temperature range in a practical manner. Therefore, this project proposes adapting and refining the conduction-cooling technologies developed in the MRI industry by keeping the field windings stationary. This paper describes the design and demonstration of a practical, cost-effective wind-and-react coil employing a simple racetrack structure and high-performance Nb_3Sn. A successful bench test will retire risk from this aspect of the design and further the concept to a higher technological readiness level (TRL).

Manuscript received XX; accepted XX. Date of publication XX. This work was supported as part of a NASA LEARN project: Grant NNX15AE41A.

David Loder is with the Electrical Capability Group at Rolls-Royce North American Technologies Inc. (LibertyWorks), Indianapolis, IN 46241 (email: david.loder@rolls-royce.com).

Matthew Feddersen, Reed Sanchez, and Kiruba Haran are with the Department of Electrical and Computer Engineering at the University of Illinois at Urbana-Champaign, Urbana, IL 61820 (e-mail: kharan@illinois.edu).

Mike Sumption, Chris Kovacs, Milan Majoros, and E.W. Collings are with the Center for Superconducting and Magnetic Materials under the Department of Materials Science and Engineering at The Ohio State University, Columbus, OH 43210.

David Doll, Xuan Peng, and Jinji Yue are with Hyper Tech Research Inc., Columbus, OH 43228.

II. Test Coil Design

A. Electromagnetic Design Selection

A representative design has been selected for the sample coil, providing a good compromise between wire usage, armature flux density, and active shielding. However, the dimensions are slightly scaled down in order to fit in the available cryostat. The full-size coil is expected to produce 2.5 T airgap field in a full machine [1]. The coil is wound using a high-performance tube type Nb_3Sn strand (tracer number 1581) which has 180 filaments and an OD of 0.7 mm [12]. The field distribution of the single test coil taken from this design is shown in Fig. 1. The results from a 3-D finite element analysis (FEA) are used to determine the magnet load line. The intended operation point is at a 50% safety margin within the critical surface (I_{op}/I_c = 435 A / 850 A), at a peak field of 6 T at 4.2 K.

B. Coil Former

The support structure is shown in Fig. 2. The coil is wound around a copper former and copper thermal buses are included on each side of the coil to connect to the cryocooler and evenly distribute the cooling. The assembly is then encased in supporting steel structures. The shrinkage of the steel at cryogenic temperatures also provides some compressive prestress to the winding, which is critical in maintaining the conductor below its strain tolerance [13]. The terminal block

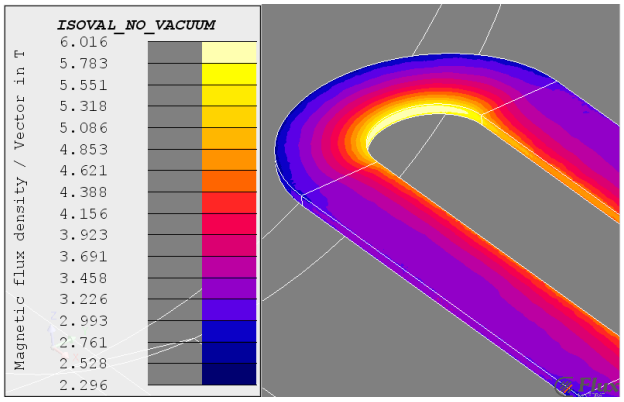

Fig. 1. 3-D FEA plot of flux density magnitude at the operational current of 435 A. Peak fields of 6 T are produced. The magnet load line suggests that near 8 T can be reached at the critical current.

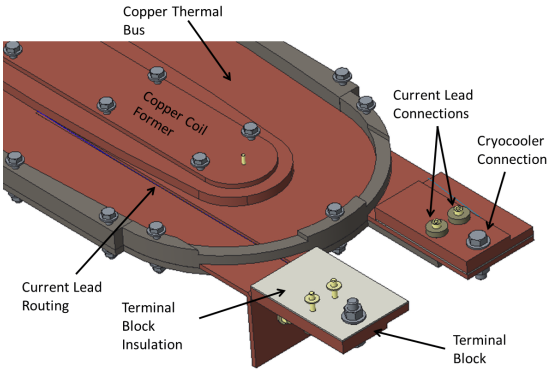

Fig. 2. Coil former and winding support structure. The setup is designed as to emulate as closely as possible the environment seen by the coil inside the full machine.

is mounted right above the cryocooler connection, providing cooling through the electrical insulation piece.

1) Thermal Analysis: The main heat loads to the superconducting coil consist of radiation from the cryostat, as well as resistive heating within the current leads. Heat conduction is not taken into account since the test setup rests on a highly insulated fiberglass surface. To mitigate radiation heat load, a two-stage cryocooler is used to thermally anchor a radiation shield near 60 K. The second stage is used to cool the coil to near 4.2 K. Based on current lead and junction resistance estimates, the heat load generated by the current leads is calculated to be 0.5 W.

Emmissivites for the appropriate materials, such as stainless steel, are found in [14]. The radiation shield is considered to be a gray body; thus, the radiation heat load is given by

$$\dot{Q} = \frac{\sigma(T_1^4 - T_2^4)}{\frac{1-\epsilon_1}{A_1\epsilon_1} + \frac{1}{A_1 F_{1\to 2}} + \frac{1-\epsilon_2}{A_2\epsilon_2}} \tag{1}$$

where σ is the Stefan-Boltzmann constant, ϵ is the emissivity of each body, A is the surface area of each body, and $F_{1\to 2}$ is the view factor from surface 1 to surface 2.

Material properties, specifically thermal conductivities of the various former materials, are taken from [15] and [16]. The thermal conductivities of the Nb_3Sn and the s-glass were found from [17] and [16], respectively. The thermal conductivity of

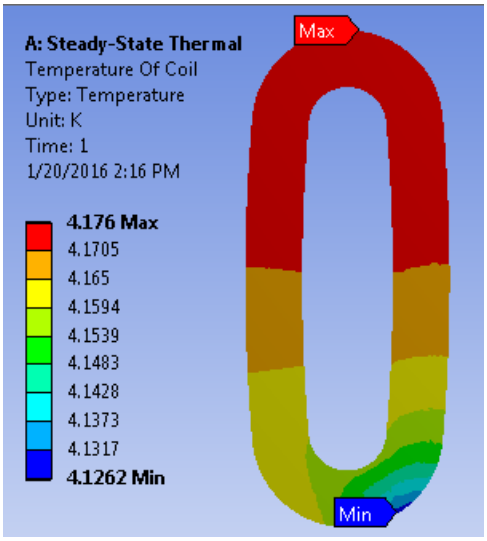

Fig. 3. Steady state temperature distribution on racetrack coil. Simulation done with only one cryocooler connection on the bottom left of the coil.

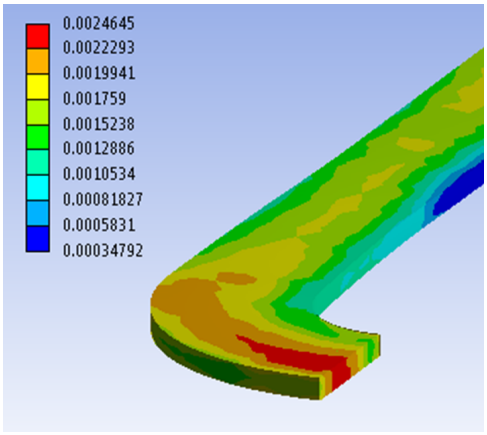

Fig. 4. Distribution of the vector strain magnitude in the end region of the coil. The strain is almost entirely compressive due to the thermal pre-stress.

the coil is found by solving Eq. (2) for K_{eq}, resulting in Eq. (4).

$$R_{eq} = R_{epoxy} + R_{S-Glass} + R_{Nb_3Sn} \tag{2}$$

$$\frac{L_{eq}}{A * K_{eq}} = \frac{L_{epoxy}}{A * K_{ep}} + \frac{L_{S-G}}{A * K_{S-Glass}} + \frac{L_{Nb_3Sn}}{A * K_{Nb3Sn}} \tag{3}$$

$$K_{eq} = \frac{L_{eq}}{\frac{L_{epoxy}}{K_{ep}} + \frac{L_{S-G}}{K_{S-Glass}} + \frac{L_{Nb_3Sn}}{K_{Nb_3Sn}}} \tag{4}$$

A thermal FEA analysis was then performed using ANSYS; an iterative solution incorporating cryocooler load curves [18] produces a heat distribution shown in Fig. 3. Heat flow is estimated at 0.59 W, with a maximum temperature of 4.17 K. Lumped thermal model analysis achieves similar results within 1% error.

2) Structural Analysis: To avoid excessive performance degradation, the maximum tensile strain within the coil must be contained below 0.2% based on manufacturer data, and the maximum compressive strain below 0.5% [19]. Stresses arise

not only from large Lorentz forces generated within the coil, but also from thermal compression resulting in shrinkage of the steel enclosure. Both of these stress sources have been modeled in ANSYS with an integrated thermal and structural FEA. The resulting strain distribution is shown in Fig. 4. Broken down into components, maximum strain parallel to the wire-epoxy matrix was found to be 0.01%, and maximum transverse compressive strain was found to be 0.25%, both of which are well within limits.

The material properties used for these analyses are summarized in Table I. The Young's Modulus of the Nb_3Sn was taken from [21]. Each constituent material exhibits nonlinear behavior in terms of the thermal conductivity and coefficient of thermal expansion (CTE) [16] [17]. The values listed in Table I are given at the anticipated operating temperature of 4.2 K; changes in thermal properties due to temperature deviations are determined with a linear interpolation around this point. Variability in the manufacturing process can result in widely varying thermal properties for the Nb_3Sn strand; a conservative value has been included in Table I (i.e. a low value for thermal conductivity) [17]. Each constituent material has isotropic material properties, but when taken as a composite material, the wire-epoxy matrix exhibits orthotropic properties which differ in the longitudinal direction (along the direction of the wire), and the transverse direction. An orthotropic tensor of the wire-epoxy matrix properties was calculated with a mass-averaging. The equivalent thermal conductivity was calculated by modelling an equivalent thermal resistance network, with thermal resistors in parallel for the longitudinal direction, and in series for the transverse direction. The equivalent CTE was computed in the same manner. Conversely, the Young's Modulus was modelled with branches in series for the longitudinal direction, and in parallel for the transverse direction. The fill factor of the strands (defined as the ratio of the total uninsulated strand area to the coil cross-sectional area) was assumed to be 50%. After winding and manufacture, the resulting fill factor was calculated to be 53.8%.

TABLE I
COIL MATERIAL PROPERTIES

	Nb_3Sn	Composite	Copper	SS316
Thermal Conductivity (W / m · K)	100	74	400	13.8
Coefficient of Thermal Expansion ($^\circ C^{-1}$)	-2.0e-3	-2.1e-3	-3.3e-3	-3.0e-3
Emmisivity (Unitless)	N/A	N/A	N/A	0.4
Young's Modulus (GPa)	121	41	110	190

Note: All temperature-dependent material properties are given for the assumed operating temperature of 4.2 K. The composite column refers to the mass-averaged material properties of the wire-epoxy matrix.

TABLE II
COIL CONSTRUCTION DETAILS

Materials	
Former	Copper with Insulating Coating
Outer Cover	316 Stainless Steel
Wire	
Strand	Nb_3Sn
Insulation	S-Glass
Number of Filaments	180
OD Bare Wire	0.7 mm
OD with Insulation	0.8 mm
Non-Cu	46.5%
Heat Treatment	625 °C / 120 h, Vacuum

III. HARDWARE VALIDATION

A. Construction

The coil was constructed with the wind and react method. After the separate former components were machined, they were sprayed with an insulating coating and assembled. Details of the coil construction are found in Table II. The wire was then wound around the former until it lay flush with the intended location of the steel supporting pieces. After the steel supports were bolted, the entire coil was heat treated, and then vacuum impregnated with a commercially available epoxy. The strand leads were secured during heat treatment using a screw. Without prior experience of a coil of this scale, wire expansion during heat treatment was greater than expected, causing the wire to bend appreciably (Fig. 5). The expansion posed a problem on the bottom current lead, where this wire bent enough to move off the terminal block (Fig. 6). Rather than moving the brittle strand post heat treatment, a copper extension was soldered to the terminal block to provide a thermal connection. This was an important learning experience for the manufacture of large racetrack coils. For future builds, the strand will be secured using a different method that allows the wire to expand directly outwards, such as a sheath that the strand is run through.

B. Experimental Setup

The coil was instrumented with voltage, temperature, and field effect sensors as shown in Fig. 7. While the test coil was originally meant to be cryocooled, maintenance issues with the equipment did not allow the coil to go below 10 K with the intended setup. An alternate setup was then pursued, which is shown in Fig. 8. The coil is shown vertical, and wrapped with super-insulation. It sits on a G10 plate, which itself hangs from threaded rods from the top of the dewar. The coil is also mechanically fixed by pressure rods coming in from the threaded rods holding the coil up. The current lugs are at the coil top. The Cernox sensor at the bottom was attached on the cooling rod and also acted as a helium filling level indicator. An additional pair of copper busbars runs to the top of the dewar, and cables (yellow) also cool the leads directly.

While liquid helium is used as a heat sink, it still mimics the conduction cooling because only a small pool of helium is used to heat station the copper tabs and current leads that were originally meant to be connected to the cryocooler. In this manner, this setup is still a reasonable test of the coil heat extraction system. Unfortunately, the cryostat available for this

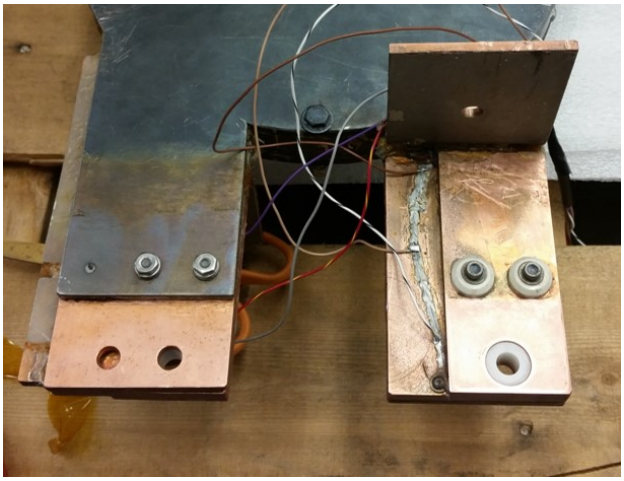

Fig. 5. Top current lead of the racetrack coil. Heat treatment caused an expansion of the wire, which caused the strand to bend outwards.

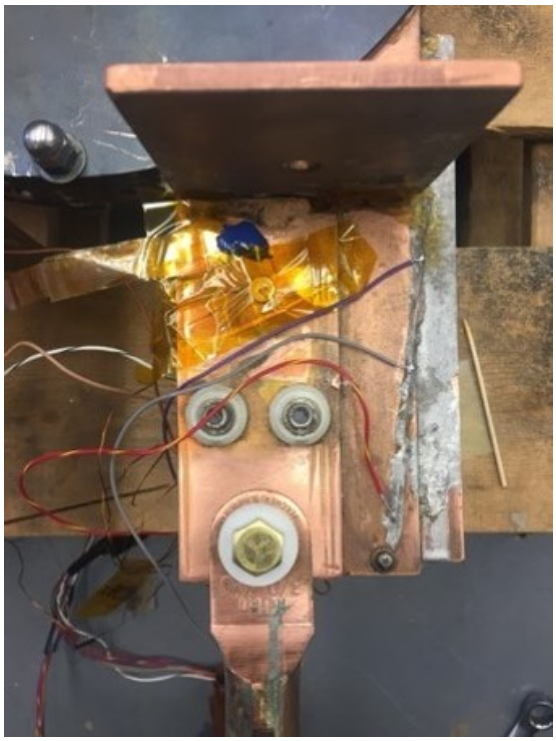

Fig. 6. Bottom current lead. Here the wire bent outwards off of the terminal block. To provide thermal connectivity without risking damage to the wire, a copper extension was soldered to the terminal block.

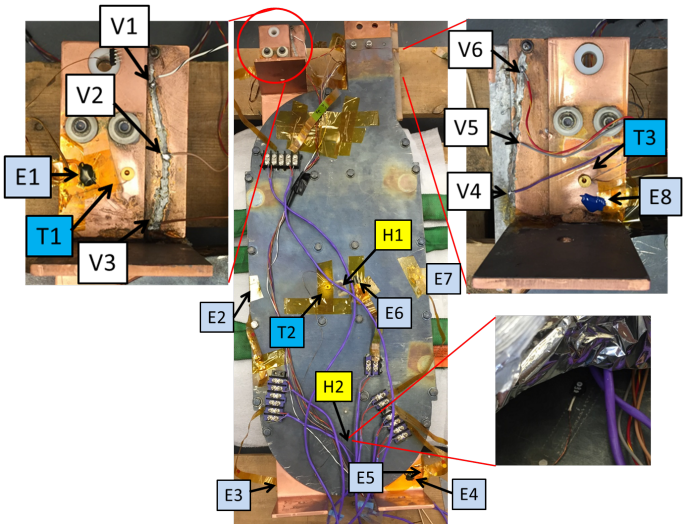

Fig. 7. Coil instrumentation. Voltage taps are indicated by white V1-V6. Cernox temperature sensors are indicated by dark blue T1-T3 [20]. Type E thermocouples are indicated by light blue E1-E7. Hall effect sensors are indicated by yellow H1-H2.

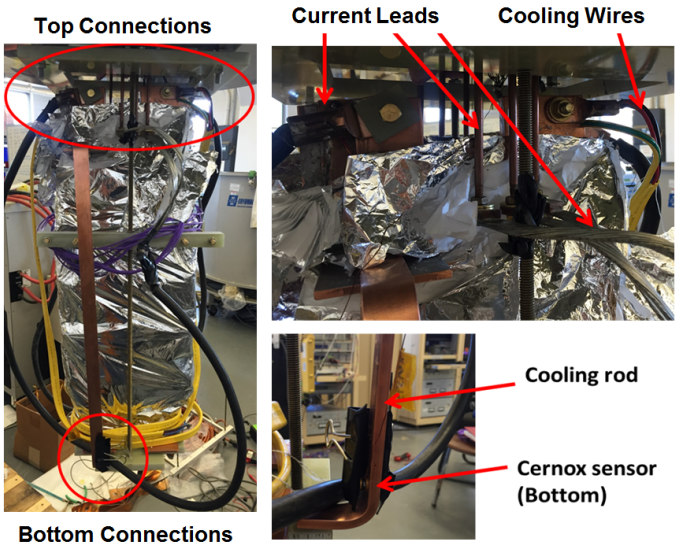

Fig. 8. Coil setup for quasi-conduction cooling using liquid helium. Coil is suspended vertically by resting on a G10 plate that is anchored to the lid of the cryostat. The bottom copper tabs are immersed in a small pool of helium at the bottom, and the current leads are heat stationed with the helium before they connect to the terminals.

setup does not have thermal shielding on the top lid. Therefore, radiation heat loads are expected to be much higher than the coil would experience in the full machine; this is manifest in the large temperature difference between the coil center (4.6 K) and the hotspot at the current leads (6.8 K), as seen in Table III.

C. Test Results

The coil was placed in the dewar and then liquid nitrogen was slowly injected at the bottom of the dewar to cool the coil by gas and thermal conduction overnight. The nitrogen was left to boil off, and then a liquid helium fill was initiated, with liquid taken to the bottom of the dewar. The cool down curves are shown in Fig. 10. After cooling, a few inches of liquid helium were allowed to accumulate at the bottom of the dewar, but below the coil. The helium cooled the conduction feet of the dewar, as well as the busbar, and these cooled the coil by conduction.

Four separate tests were conducted on the coil. In all tests except Run #3, current was applied using voltage mode to prevent the possibility of overvoltage. In Run #3, current-controlled mode was used in order to capture a flat I-V curve, as seen in Fig. 9. The initial ramping rate was 1 A/s. Then, it reduced to 0.8 A/s near 300 A. This latter is the reason for the

TABLE III
CERNOX TEMPERATURE READINGS AND CRITICAL CURRENT

	Run 1		Run 2		Run 4	
	Coil Center	Current Tap	Coil Center	Current Tap	Coil Center	Current Tap
Initial Temp. (K)	4.53	6.54	4.67	5.78	4.67	6.81
Temp. at Quench (K)	4.66	7.38	4.74	7.18	4.84	7.92
ΔT (K)	0.13	0.84	0.07	1.4	0.17	1.11
Critical Current (A)	437		440		480	

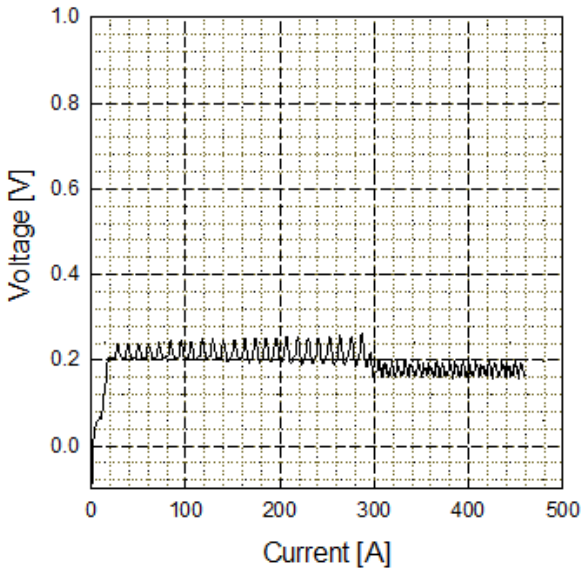

Fig. 9. I-V data for Run 3 in current-controlled mode. Some offset is seen due to the inductive voltage, which changes when the ramp rate is modified after 300 A is reached.

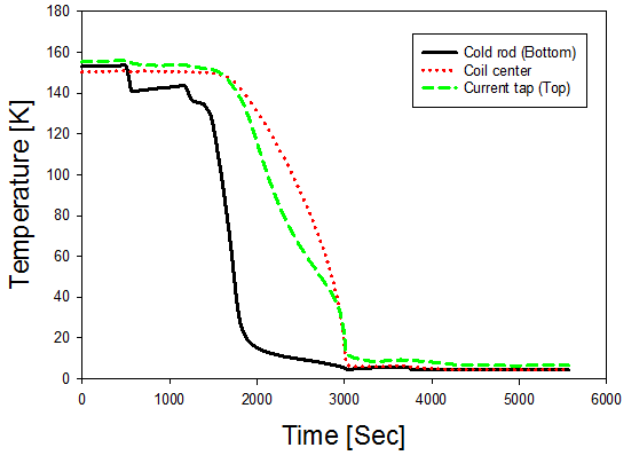

Fig. 10. Cooldown of the coil before test. Notice that the current leads cool more quickly than the center of the coil surface, indicating an excellent thermal connection between the leads and the cooling tabs. After cooldown, the maximum temperature difference across the coil with no current applied was 2.25 K (4.2 K to 6.45 K).

change in noise and inductive offset at 300 A. The maximum take-off-voltage trigger was set at the voltage of 300 mV.

For the voltage-controlled test runs, the ramping rate was 0.01 V/s, and the average ramping rate above 400 A was 1.1 A/s. The maximum take-off-voltage trigger was set at the voltage of 1 V. Results from Run #4 are shown in Fig. 11, where we can observe a temperature increase at the current terminals as the current increases; this was due to the solder contacts at the current lead to superconductor interface, and could be reduced by additional cooling, or reducing contact resistance. The transition was by quench, not unexpected for an LTS coil running at high currents to I_C in conduction cooled mode. Temperature data and critical current for the three voltage-controlled runs are shown in Table III. The critical current capability increased after each run, due to magnet training. The highest critical current achieved was 480 A, which surpassed the intended operational current of 435 A. The field data are plotted against numerical model predictions in Fig. 12. Results agree well with the model, giving confidence to the projected peak field of 5.85 T in the coil end winding.

To examine the temperature margin of the coil, heat was injected to measure critical current at increasing temperatures.

TABLE IV
CRITICAL CURRENT RECORDED WITH VARYING TEMPERATURE

Run	Temp. Coil Center (K)	Temp. Coil Top (K)	I_C/I_Q (A)	On-Axis Field (T)
4	4.84	6.81	480	2.20
5	5.56	7.53	457	2.09
6	8.02	9.99	384	1.75
7	10.83	12.8	265	1.20

Three more test runs were taken, with results in Table IV. Temperature dependence is shown graphically in Fig. 13, with the critical current projected at 4.2 K. In the full machine, with proper radiation shielding, it is expected that the hotspot temperature will be much closer to this ideal value. If this can be achieved, the predicted critical current of 550 A would yield a 26% margin with respect to the operational current of 435 A, meaning the coil could be very safely operated at this current allowing some margin for AC losses due to transient conditions. Thus, much of the risk associated with manufacturing a high-field conduction cooled coil has been mitigated.

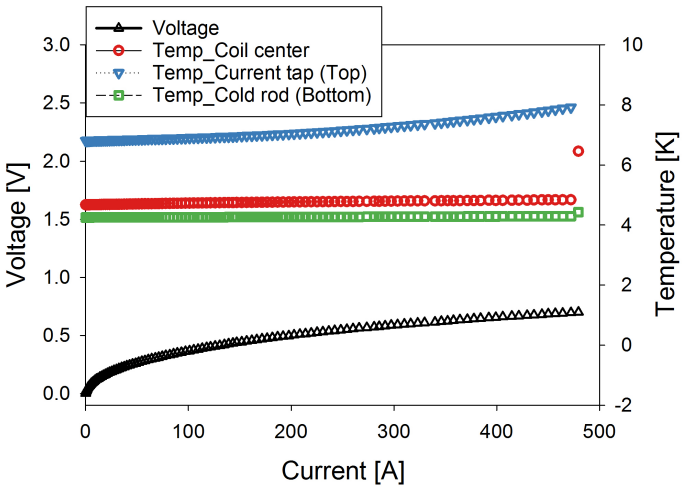

Fig. 11. Temperature measurements during the final test run in voltage control mode. Critical current reached 480 A at quench. A temperature rise due to ohmic heating in the current leads is observed near 1.1 K.

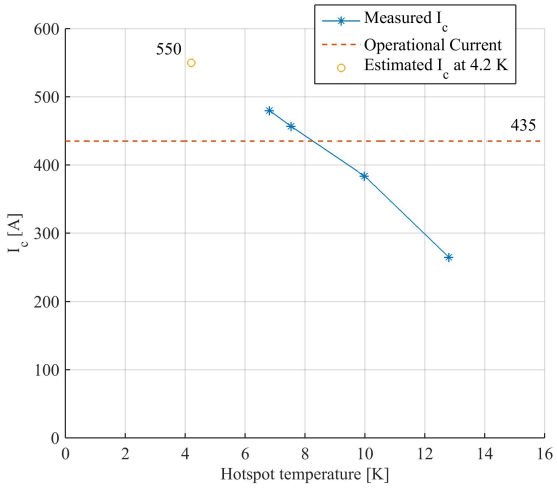

Fig. 13. Critical current vs. hotspot temperature. Ic at 4.2 K is estimated at 550 A. Compared to the desired operation at 435 A, this corresponds to an operational margin of 26% Similarly, the temperature margin is substantial at 4.1 K.

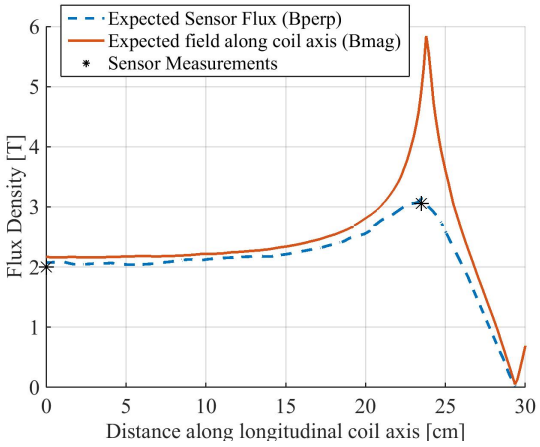

Fig. 12. Collected field data vs. expected value from 3-D FEA. Sensor data matches simulation results with less than 4% error. Peak field within coil is expected to be 5.85 T, based on the simulation.

TABLE V
TEST COIL SCALING COMPARISON

	Full-size coil	Test coil
Dimensions		
Coil aperture	106.2 mm	96.7 mm
Winding pack height	78.4 mm	70.7 mm
Winding pack width	10.5 mm	9.5 mm
Active length	437 mm	380 mm
No. turns	1152	957
Total conductor length	1555 m	1209 m
Turns/layer	12	11
No. layers	96	87
Performance Metrics		
Peak field	6.2 T	6 T
Strand current	420 A	435 A
Eng. current density (Je)	587 A/mm^2	620 A/mm^2
Peak stress	40.8 MPa	37.5 MPa

D. Discussion

Although the final coil was tested in a quasi-conduction cooled mode, the test was closely representative for the peak fields and stress that a full-size coil would see. Table V highlights the prime differences between the finalized test coil and the intended full-size coil that would be used in the machine. Peak stresses are within 10% of the full-size coil. This bench test was also a good opportunity to prove out the construction of a large conduction-cooled Nb_3Sn magnet, and valuable lessons were learned.

Because of the unexpected issues with the cryocooled setup, the test did not yield a good replication of the radiation heat loads that would be experienced by the coil in the full machine. Furthermore, there remains the untested aspect of conduction due to connecting structural members such as the torque tube. These issues are being targeted for future work as the next key risk to address.

IV. Conclusion

In this paper, the process for the design of a superconducting coil, and a process for its bench test was described. FEA analysis and prior optimization work was used to select critical current and field targets. Then, a support structure for the coil windings was designed, and its thermal and structural interactions with the coil were analyzed. The coil was instrumented and then energized to test critical current capability. A small reservoir of liquid-helium was used to imitate cryocooler thermal connections. Due to equipment constraints, the radiation heat load seen by the test coil was much higher than planned. However, the coil surpassed performance targets even at higher temperatures of 7.9 K. The current capability demonstration gives confidence that, when properly shielded, the coil will be able to operate at desired currents with a reasonable safety margin (26%). Future work is planned to more accurately capture heat load and cooling conditions seen within the full machine design.

REFERENCES

[1] D. C. Loder and K. S. Haran, "Multi-objective optimization of an actively shielded superconducting field winding: Pole count study," in *Proc. IEEE Int. Electric Machines Drives Conf. (IEMDC)*, May 2015, pp. 1709–1714.

[2] K. S. Haran, D. Loder, T. O. Deppen, and L. Zheng, "Actively shielded high-field air-core superconducting machines," *IEEE Trans. on Appl. Supercond.*, vol. 26, no. 2, pp. 98–105, Mar. 2016.

[3] R. D. Rosario, "A future with hybrid electric propulsion systems: A nasa perspective," in *Turbine Engine Technology Symposium*, Dayton, OH, Sep 2014.

[4] G. Sabbi *et al.*, "Design of HD2: a 15 tesla nb_3sn dipole with a 35 mm bore," *IEEE Trans. on Appl. Supercond.*, vol. 15, no. 2, pp. 1128–1131, Jun. 2005.

[5] S. Caspi *et al.*, "Fabrication and test of tqs01 —a 90 mm nb_3sn quadrupole magnet for larp," *IEEE Trans. on Appl. Supercond.*, vol. 17, no. 2, pp. 1122–1125, Jun. 2007.

[6] R. Gupta *et al.*, "React and wind nb_3sn common coil dipole," *IEEE Trans. on Appl. Supercond.*, vol. 17, no. 2, pp. 1130–1135, Jun. 2007.

[7] P. Ferracin *et al.*, "Development of mqxf: The nb_3sn low- quadrupole for the hilumi LHC," *IEEE Trans. on Appl. Supercond.*, vol. 26, no. 4, pp. 1–7, Jun. 2016.

[8] J. C. Perez *et al.*, "16 T nb_3sn racetrack model coil test result," *IEEE Trans. on Appl. Supercond.*, vol. 26, no. 4, pp. 1–6, Jun. 2016.

[9] F. Savary *et al.*, "Status of the 11 T dipole project for the LHC," *IEEE Trans. on Appl. Supercond.*, vol. 25, no. 3, pp. 1–5, Jun. 2015.

[10] Y. Lvovsky *et al.*, "Novel technologies and configurations of superconducting magnets for MRI," *Superconductor Science and Technology*, vol. 26, no. 9, p. 093001, 2013.

[11] W. Stautner and S. Mine, "A cryo-free 10 T high-field magnet system for a novel superconducting application - experimental results," *IEEE Trans. on Appl. Supercond.*, vol. 22, no. 3, pp. 3–7, 2012.

[12] M. Sumption, S. Bhartiya, C. Kovacks, X. Peng, E. Gregory, M. Tomsic, and E. Collings, "Critical current density and stability of Tube Type Nb_3Sn conductors," *Cryogenics*, vol. 52, no. 2-3, pp. 91–99, 2012.

[13] B. ten Haken, A. Godeke, and H. H. J. ten Kate, "The strain dependence of the critical properties of Nb_3Sn conductors," *J. Appl. Phys.*, vol. 85, no. 6, pp. 3247–3253, 1999.

[14] N. H. Balshaw, "D8 Cryostats," in *Handbook of Applied Superconductivity*. Institute of Physics Publishing, 1998.

[15] R. A. Matula, "Electrical resistivity of copper, gold, palladium, and silver," *J. Phys. Chem.*, vol. 8, no. 4, 1980.

[16] J. Jensen, W. Tuttle, R. Stewart, H. Brechna, and A. Prodell, "Material properties important to the design of a large superconducting magnet," Brookhaven National Laboratory, Tech. Rep. BNL 10200-R, Vol. I, Aug 1980.

[17] M. Bonura and C. Senatore, "Thermal conductivity of industrial Nb_3Sn wires fabricated by various techniques," *IEEE Trans. on Appl. Supercond.*, vol. 23, no. 3, Jun. 2013, Art. no. 6000404.

[18] Sumitomo RDK415 Cryocooler Load Map. Janis. [Online]. Available: http://www.janis.com/Libraries/4K_Coldheads/RDK415D_cryocooler_dwg_loadmap.sflb.ashx

[19] L. Summers, J. Miller, and J. Heim, "The International Thermonuclear Exprimental Reactor (ITER) Design and Materials Selection," Lawrence Livermore National Laboratory, Tech. Rep., 1989.

[20] (2016) Sensor selection guide. Lake Shore Cryotronics. [Online]. Available: http://www.lakeshore.com/Documents/LSTC_sensorselection_l.pdf

[21] M. Hojo *et al.*, "Direct measurement of elastic modulus of Nb_3Sn using extracted filaments from superconducting composite wire and resin impregnation method," *Physica C*, vol. 445-448, pp. 814–818, Oct. 2006.